Nano to macro transition of gold nanoparticles prior to sintering

Paige Summers[1], Alexander Angeloski[1], Michael B. Cortie[2], Richard Wuhrer[3], and Andrew M. McDonagh[1,*]

[1] *School of Mathematical and Physical Sciences, University of Technology Sydney, Broadway, Ultimo, NSW 2007, Australia*

[2] *5 Hazel Crescent, Thirroul, NSW 2515, Australia*

[3] *Advanced Materials Characterisation Facility (AMCF), Western Sydney University, Locked Bag 1797, Penrith, NSW 2751, Australia*

ABSTRACT

The thermal behaviour of ligand-stabilised gold nanoparticles (AuNPs) is an important consideration when using these materials to form gold films via sintering. AuNPs stabilised with butanethiol and hexadecanethiol ligands displayed quite different properties upon heating up to their sintering temperatures. Films of AuNPs bearing the longer chain stabilising ligand hexadecanethiol become liquids at 56 °C. This temperature corresponds to the melting point of dihexadecyl disulfide, a known product that forms when such AuNPs are heated. No liquid phase was observed for butanethiol-stabilised AuNPs at any temperature. Films of the hexadecanethiol-stabilised AuNPs had high resistances (> 100 MΩ) at room temperature and the short-chain butanethiol-stabilised AuNPs had resistances in the kΩ range. Small-angle X-ray scattering data showed that the butanethiol-stabilised AuNPs begin to coarsen at ~ 140 °C whilst the hexadecanethiol particles began to coarsen ~ 90 °C.

1 Introduction

The sintering of gold nanoparticles (AuNPs) is a convenient technique for the formation of electrically conductive gold films and additively manufactured gold-based materials and devices [1–3]. Sintering involves the coalescence of particles at temperatures below their melting point, which in the case of bulk gold is 1064 °C [4]. The AuNPs can be formulated as printable inks that can be printed using either contact or non-contact printing techniques, and then sintered at moderate temperatures (usually around 200 °C) to form the desired gold structures [1, 5, 6]. Prior to sintering, the AuNPs must be stabilised to prevent unwanted aggregation or coalescence, which would otherwise render printable inks unusable. A number of stabilisers have been investigated including ionic compounds (e.g. citrate) [7, 8], polymers (e.g. polyvinyl pyrrole) [9], and of particular relevance to this work, thiol compounds [10].

Thiol-protected AuNPs have shown to be accessible, reproducible, stable and have a large range of tuneable sintering temperatures [11–17]. The interaction of the sulfur atoms with the gold surface may be described as a thiyl-gold species (where thiyl is the •SR radical species). That is, the thiol (H-SR) species is deprotonated

🍀 Springer

upon binding to the gold surface. From studies of self-assembled monolayers, an equilibrium was described between gold surface-bound thiyl species and the corresponding unbound disulfide compounds (RS-SR) [18]. Thus, upon sintering, the stabilising ligands are released as the disulfide species, with the volatility of the disulfide influencing the temperature of the sintering event (T_{SE}) [15]. However, the properties of such thiol-stabilised AuNPs have been less studied in the temperature range immediately prior to and during the sintering transition [19]. For amine-stabilised AuNPs, coarsening behaviour prior to sintering has been reported at temperatures approaching the T_{SE} (by observation of optical properties and scanning electron microscopy (SEM)) [20]. Here we examine the behaviour of thiol-stabilised AuNPs (using a short- and long-chain stabilising alkanethiol) in the temperature regime from room temperature to sintering using SEM, in situ synchrotron small-angle X-ray scattering (SAXS) techniques, and electrical resistance measurements. The electronic conductivity of films of alkanethiol stabilised AuNPs offers insights into their structures. Between individual NPs, the conductivity has been shown to occur due to electron tunnelling between the gold cores via the alkanethiolate chains [21]. Previously, the electrical conductivity for films of gold nanoparticles was observed to increase irreversibly upon heating to temperatures below those of T_{SE} and the activation energies were found to change dramatically following a single heating cycle [22].

We build upon our previous investigations that demonstrated the effect of the volatility of dialkyl disulfide compounds that form during heating on the sintering behaviour of thiol-stabilised AuNPs [12, 15, 23]. Here, we use electrical resistance measurements, SAXS and SEM to examine thiol-stabilised AuNPs at temperatures from room temperature up to their T_{SE} to better understand the processes that lead from the nanoscale to macroscale gold films.

2 Experimental

1-Butanethiol, 1-hexadecanethiol, tetraoctylammonium bromide, sodium borohydride, and methanol were purchased from Sigma-Aldrich and used as received. Toluene (ChemSupply Australia) and chloroform (Rowe Scientific) were used as received. Tetrachloroauric acid [24], butanethiol AuNPs (BT@AuNPs), and hexadecanethiol AuNPs (HDT@AuNPs) were prepared using literature procedures [25]. The AuNPs were characterised by SEM, transmission electron microscopes (TEM), and ultraviolet–visible (UV–vis) absorption spectroscopy.

Resistance measurements of AuNPs suspensions of BT@AuNPs in chloroform (10 mg/ml) were drop cast onto DropSens (Metrohm) interdigitated gold electrodes forming films of AuNPs, which were then heated using a modified Linkam THMS600 temperature control stage as described previously [15]. A heating rate of 10 °C min^{-1} from room temperature to 250 °C was used. A Rigol DM3068 digital multimeter with a maximum resistance measurement capability of 100 MΩ was used to measure electrode resistances. A LabView program was used to acquire the temperature and electrical resistance data. SEM was performed at facilities at Western Sydney University, Australia. A Zeiss Merlin field emission gun scanning electron microscope (FEGSEM) was utilised for imaging samples prepared on stubs. The FEGSEM was operated at 10 kV accelerating voltage in Hivac mode at a working distance of approximately 3 mm. Both secondary and in-lens secondary detectors were utilised for imaging. TEM images were taken using a JEOL JEM-F200 FE-TEM operating at 200 kV and fitted with a Gatan Rio 1816—4 k × 4 k camera. The TEM samples were prepared by evaporating diluted nanoparticle solution on the carbon-coated copper grid. The images were analysed using ImageJ software (https://imagej.nih.gov/ij/). UV–Vis spectra were recorded on an Agilent Cary 60 spectrophotometer. Samples were prepared in a quartz cuvette by dispersing ~ 0.4 mg of AuNP sample in toluene (8 mL). Variable temperature SAXS measurements were performed at the Australian Synchrotron using the SAXS/WAXS undulator source. Powders of AuNPs were placed in SiO_2 capillaries. The samples were exposed to 8×10^{12} photons per second at an X-ray energy of 11.5 keV, and scattered X-rays were detected using a Pilatus 1M detector with active area of 170 mm × 170 mm at a distance of 1400 mm. Detector images were acquired at a scan rate of 10 Hz and averaged to yield one frame for every ~ 1 °C in temperature between 30 °C to either 160 °C or 230 °C. Detector images were corrected using ScatterBrain IDL and q vs T plots were prepared using Python3. Data was not quantitatively assessed as the aggregation state of the particles could not be accurately determined, data up until formation of the liquid phase corresponds to diffraction rather than

scattering from a solution, and upon formation of liquid phase the concentration was variable.

3 Results and discussion

3.1 Synthesis

BT@AuNPs and HDT@AuNPs were synthesised using the two-phase Brust-Schriffrin method [25] and had diameters of 3.1 (± 0.9) nm and 3.5 (± 1.7) nm, respectively, (measured using TEM, Fig. S1). The UV–visible spectra of the nanoparticles (Fig. S2) contain shoulders at ~ 517 nm (BT@AuNPs) and ~ 512 nm (HDT@AuNPs), which is consistent with AuNPs with diameters previous reports [26, 27]. Importantly, no unbound thiol was detected in the ^{1}H NMR spectra of the synthesised AuNPs.

3.2 Scanning electron microscopy

Representative SEM images of films of BT@AuNPs on silicon wafer are shown in Fig. 1. Unheated films are comprised of AuNPs that are uniform in size (within the resolution of the instrument), Fig. 1a, b. Images of films that have been heated to 100 °C reveal AuNPs of similar size to the unheated particles, Fig. 1c, d. After heating to 150°C, coarsening of the AuNPs is apparent but no sintering occurs at this temperature, Fig. 1e, f. Figure 2 shows SEM images of HDT@AuNPs that have been heated to various temperatures. Unheated films contain AuNPs in a uniform layer, Fig. 2a, b, and are similar in appearance to those of BT@AuNPs.

In contrast, films of HDT@AuNPs heated to 100 and 150 °C contain deposits of a crystalline material that obscure the AuNPs, Fig. 2c–f. We have previously shown experimentally that HDT@AuNPs release exclusively dihexadecyl disulfide upon heating [15]. We attribute the deposits observed in the SEM images to increased formation of dihexadecyl disulfide upon heating, which melts at ~ 56 °C [15] and subsequently solidifies upon cooling to room temperature prior to imaging.

Upon heating to 200 °C, Fig. 2g, h, coalesced gold material is evident, and the organic material observed in Fig. 2c–f is absent. Previous thermogravimetric analysis [15] showed that dihexadecyl disulfide undergoes mass loss at 200°C, and so over the heating period of 2 h, organic material is removed from the surface. In the case of BT@AuNPs, the formed dibutyl disulfide has significantly greater volatility [15], and thus evaporates during heating as well as during SEM imaging (in the high vacuum environment) to leave no observable residue upon cooling to room temperature.

In general, the released dihexadecyl disulfide from HDT@AuNPs results in a layer of organic material on the AuNPs that increases with temperature until ~ 150 °C, whereas the more volatile dibutyl disulfide from BT@AuNPs is removed rapidly from the vicinity of the gold surfaces. Thus, the BT@AuNPs could be imaged at each intermediate temperature, with no coarsening evident until temperatures > 100 °C. Importantly, during these experiments only a small proportion of the total ligand concentration has been removed. If otherwise, the AuNPs would have sintered [15]. We note that variable temperature TEM experiments were not conducive to coarsening investigations due to the requirement of a very low density of particles for imaging.

Resistance measurements of gold nanoparticle films. The electrical resistance of solid films of thiol-stabilised AuNPs is dependent on electron tunnelling between the gold cores via the alkanethiyl ligands [21]. The technique is therefore useful to probe changes in interparticle distances in the temperature range that precedes sintering, whereupon the resistance is similar to that of bulk gold after sintering. Small changes in core size (1.6 nm vs. 2.2 nm diameters) have relatively minor effects on conductivity but increased thiol ligand carbon chain length correlates with decreased conductivity [21]. Dropcast BT@AuNP films had resistances in the range of 3–4 MΩ when maintained at 24 °C, which were stable for at least 10 h (see Fig. S3). In contrast, the resistances of dropcast HDT@AuNP films were outside the range of our instrumentation (> 100 MΩ) at 24 °C. The increased resistances of AuNPs bearing longer chain stabilising groups has been investigated by others [21, 28, 29] and is a consequence of electrons having to tunnel over greater distances.

Upon increasing the temperature to 100 °C, the resistance of BT@AuNPs decreased by several orders of magnitude (from 3–4 MΩ range to 40–50 kΩ), Fig. 3b and Fig. S4, where it remained stable for at least 5 h (Fig. S3). The HDT@AuNP films also exhibit a drop in resistance upon heating to 100 °C with the resistance changing from off-scale to ~ 80 MΩ, Fig. 3a. In contrast to the BT@AuNPs, we observed that the HDT@AuNP films become molten at ~ 56 °C. This phenomenon has been investigated previously using differential scanning calorimetry [30]. Alkylthiolate-stabilised

Fig. 1 SEM images (obtained at 21°C) of BT@ AuNPs after exposure to the following temperatures for 2 h: **a**, **b** room temperature; **c**, **d** 100 °C; **e**, **f** 150 °C
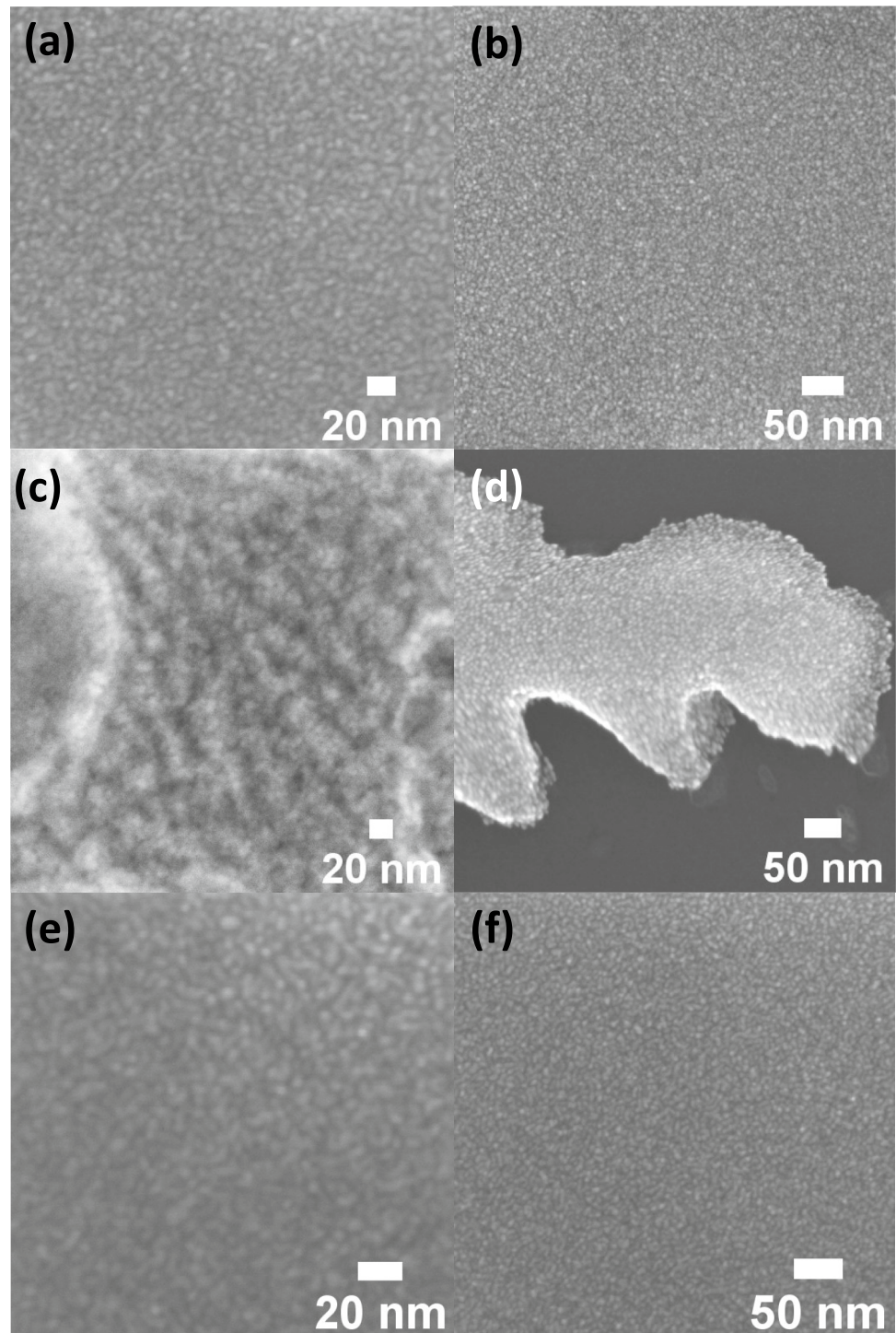

AuNPs with carbon chain lengths of 12–20 displayed phase transitions at temperatures similar to those observed here and with enthalpies that increased with increasing chain lengths [29–31]. A melting event was associated with the interdigitation of CH_2 units located ~ 10–12 units from the Au core [31]. In light of more recent findings [15], we propose that the transition to liquid phase is a consequence of the melting of the corresponding dialkyl disulfide that has been released from the NP surface. We also note that a small increase in resistance (from ~ 70 to ~ 90 MΩ) over 6 h was observed for the HDT@AuNPs and is attributed to

Fig. 2 SEM images (obtained at 21°) of HDT@ AuNPs after exposure to the following temperatures for 2 h: **a**, **b** room temperature; **c**, **d** 100 °C; **e**, **f** 150 °C; **g**, **h** 200 °C
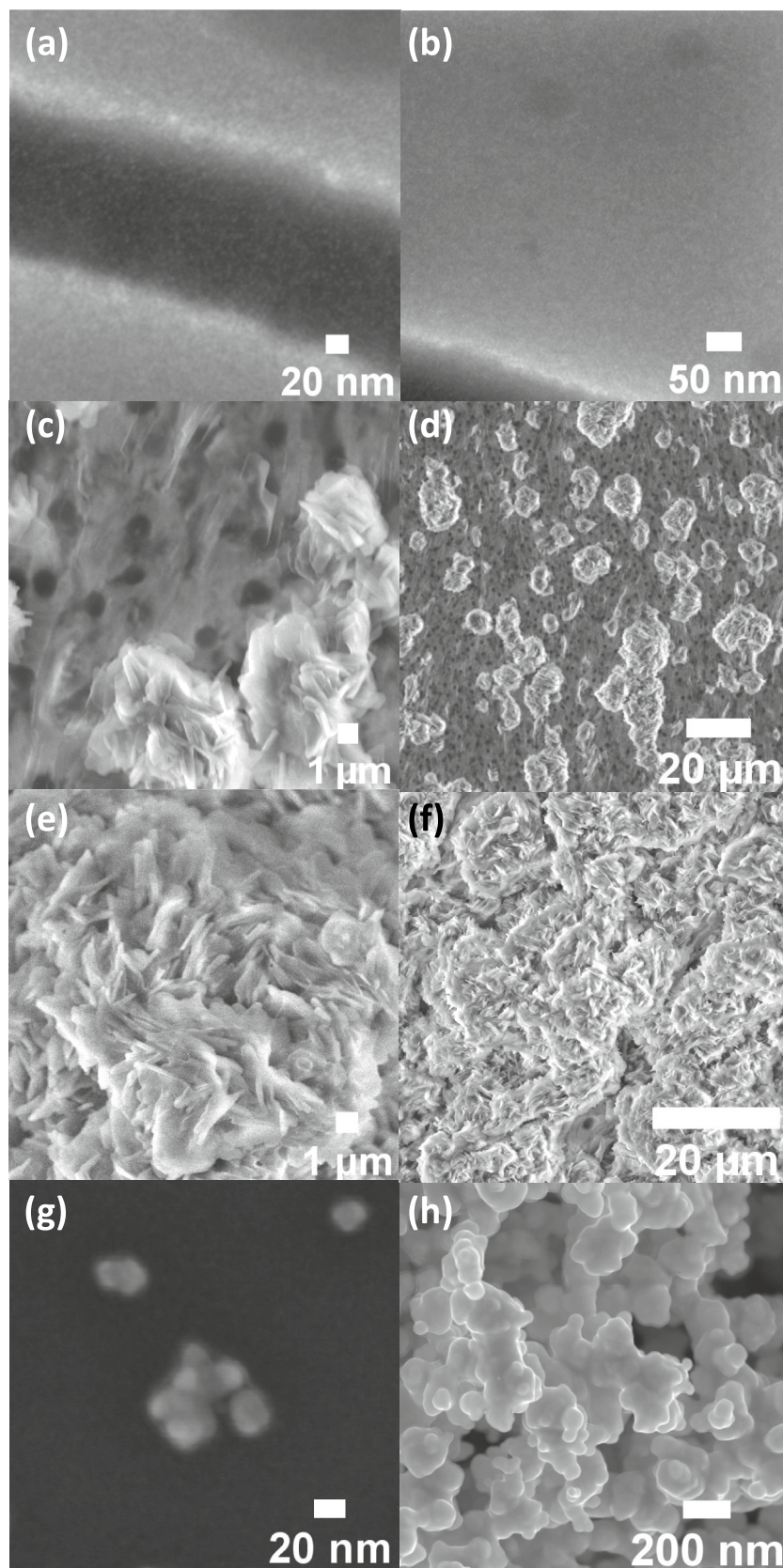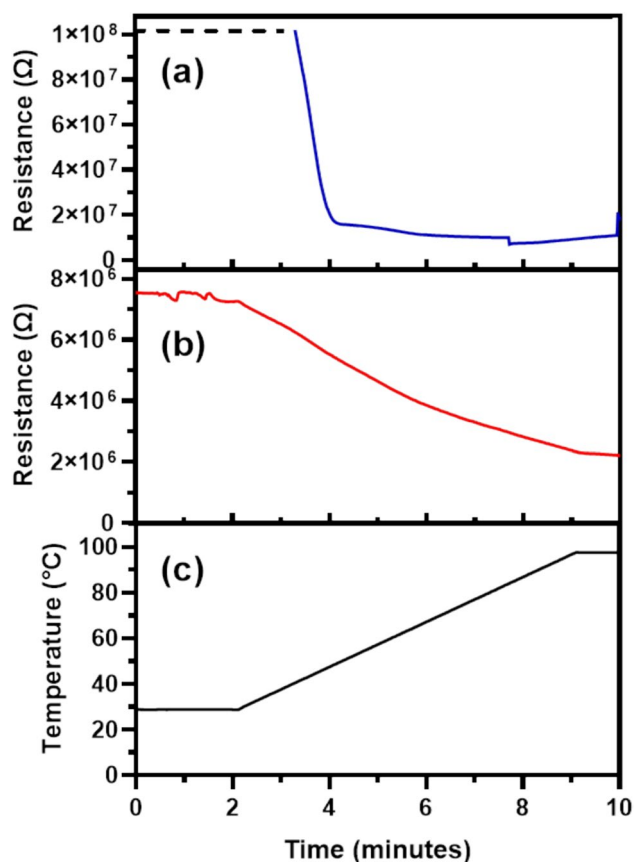
Fig. 3 Graph showing the resistances (raw data) of thiol-stabilised AuNPs during heating over a period of ten minutes. **a** HDT@AuNP film. The dotted trace for time up to 3.5 min indicates that the resistance was out of the range of the instrument (>100 MΩ). **b** BT@AuNP film. The small fluctuations up to Time = two minutes are typical of measurements of AuNPs using this apparatus [11–16]. **c** The temperature ramp used during the 10 min heating period

the fluid film expanding and thinning across the electrode surface, which was visually observed to occur.

Upon cooling the films from 100°C to room temperature, the resistances of films of BT@AuNPs did not return to the original MΩ range but increased to ~ 20 kΩ (Fig. S4) and remained stable for several hours. Re-heating the AuNP films to 180°C induced sintering at a temperature similar to that of BT@AuNP films heated directly from room temperature (T_{SE} ~ 180 °C). Our experiments indicate that changes to the AuNP film that occur upon heating to do not influence the eventual sintering process but nor do the films return to their original as-formed state, an idea proposed by others based on optical measurements [22]. This phenomenon may have electronic applications as many

AuNPs films are hindered by very high resistances at RT.

The resistance of HDT@AuNP films also increased upon cooling from 100°C to room temperature to a value that was, again, out of range of our instruments (Fig. S4), and was associated with the solidification of the films at ~ 56 °C. Re-heating to ~ 210 °C induced sintering of the HDT@AuNPs at a similar temperature to that observed for films of HDT@AuNPs heated directly (T_{SE} ~ 220 °C). We note that this type of behaviour has been reported previously [22] and it was speculated that a chemical change occurred on the particle surface.

Importantly, the resistance data shows decreases in resistance at temperatures corresponding to an increase in the gold particle size (as shown in SAXS data below). This observation suggests a shift in conductance mechanism from tunnelling (common in smaller particles) towards bulk conductance as the effective cross section of conductive gold increases [15, 21].

Small-angle X-ray Scattering. AuNPs have been previously investigated using SAXS to probe suspensions of AuNPs in a variety of solvents [32–35]. Here we present data acquired using variable-temperature synchrotron SAXS experiments on AuNP powders heated at 3 °C min^{-1}. The size of scattering elements probed was between 1 and 9 nm.

The q dependence versus temperature for BT@AuNPs, Fig. 4, shows a single constant diffraction band at $q = 0.2$ Å^{-1}, corresponding to an average spherical particle diameter of 31 Å (or 3.1 nm), which is in agreement with the measured size obtained using TEM (Fig. S1). The presence of a single band at $q = 0.2$ Å^{-1} suggests that the dispersion of the particle sizes is low. The BT@AuNPS scattering band is present with no measurable changes in intensity of FWHM until ~ 125 °C. From 125 to 140 °C, the band decreases in intensity with an associated increase in scattering from species at $q < 0.1$ Å^{-1}, which indicates a coarsening of the BT@AuNPS. Above 140 °C, all scattering signals disappear, which we attribute to the formation of particles (or aggregates of particles) >9 nm in diameter, which subsequently scatter at angles beyond the measurable range of the instrument. As the experiment temperature is less than T_{SE} for BT@AuNPs, the variable temperature SAXS clearly demonstrate the thermal stability until ~ 125 °C, at which point they coarsen into larger particles or aggregates of particles of > 9 nm in diameter. This observation is in agreement

Fig. 4 Iso-intensity map of SAXS data for BT@AuNPs heated from 30 to 165 °C at 3 °C/min
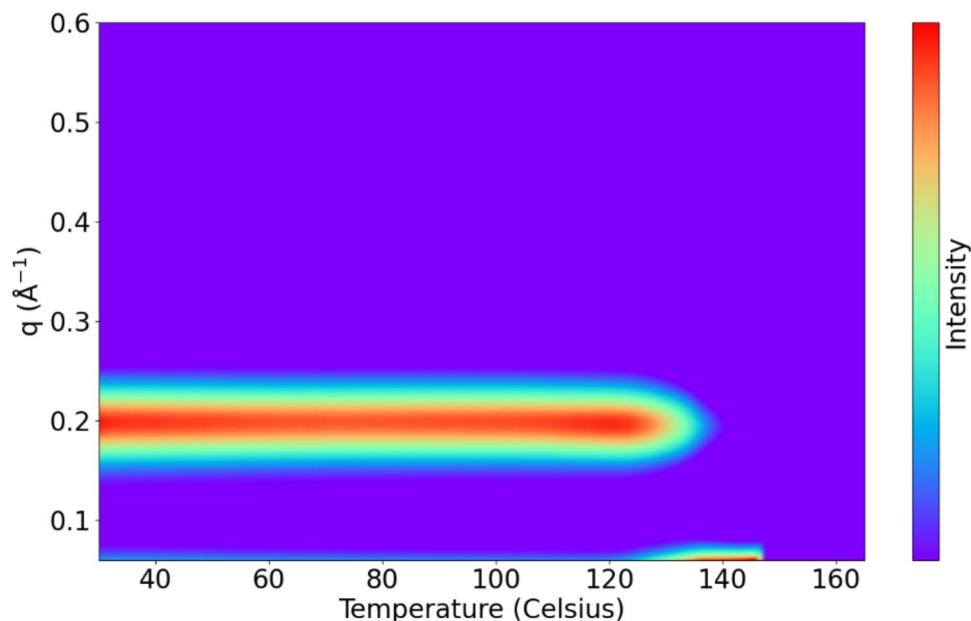
with previous studies showing an increase in the sizes of AuNPs prior to the sintering event [20] as well as the SEM observations discussed above.

For HDT@AuNPS, the scattering behaviour, Fig. 5, is different to that observed for the BT@AuNPs. At room temperature, two low intensity diffraction bands are present at q range of 0.19–0.1 Å^{-1} indicating a disperse mixture of 3.5–6 nm scattering elements. The distributions of these scatterers merge into a single band at $q = 0.12$ by ~ 40 °C, suggesting a slight coarsening of the HDT@AuNPs to a size of 5.2 nm. In the

region where the surface disulfide layer melts (~ 50 °C) the ~ 5 nm scatterers remain stable until 90 °C as indicated by diffraction bands with equal intensities between ~ 50 and ~ 90 °C. There is a sharp decrease in intensity between 90 and 110 °C and almost no intensity until ~ 160 °C, where very small amounts of scattering are observed at $q < 0.1$ indicating the presence of larger coarsened AuNPs, similar to those observed in BT@AuNPs. By 225 °C (close to the T_{SE}), all particles are larger than the q limit of the experiment. Beyond the T_{SE}, a featureless region is observed. We propose

Fig. 5 Heat map of SAXS data for HDT@AuNPs heated from 30 to 165 °C at 3 °C/min
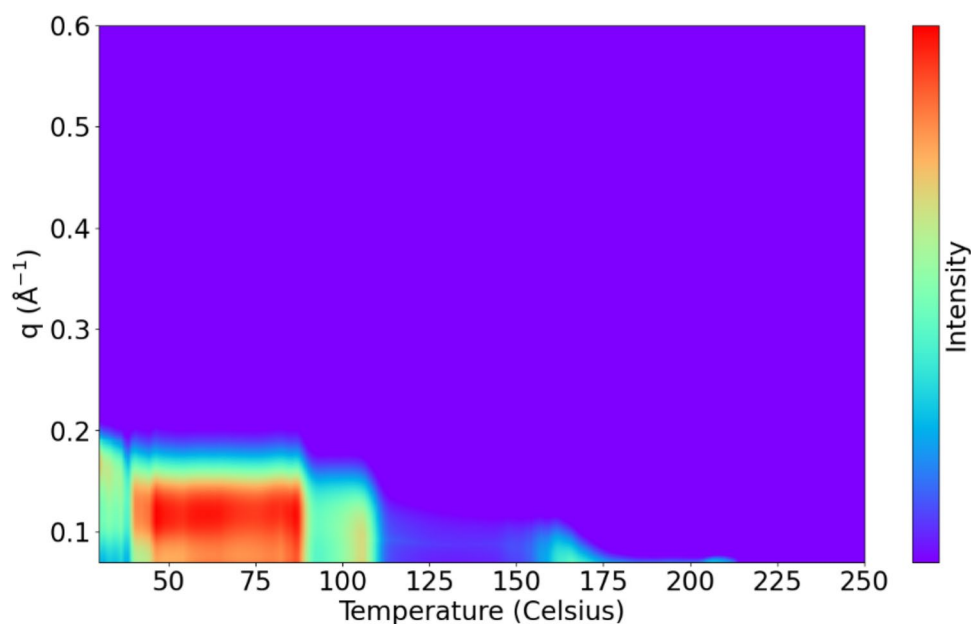
that the lack of diffraction between 110 and 160 °C is attributed to the formation of the liquid films whereby the particles are scattering in a fashion more like a solution (rather than diffraction from a solid AuNPs film). Instead, a low intensity featureless dispersion is observed until ~ 160 °C. At 160 °C, an increased intensity of scattering from species at $q < 0.1$ Å^{-1} is observed, attributable to the coarsening of the HDT@AuNPs to form scattering species > 9 nm in diameter. That is, sufficient dihexadecyl disulfide is formed from the surface of AuNPs to give a dispersion of HDT@AuNPs in dihexadecyl disulfide, from which the suspended HDT@AuNPs coarsen.

4 Conclusion

Films of AuNPs stabilised with butanethiol and hexadecanethiol ligands displayed quite different properties upon heating up to their sintering temperatures. Films of HDT@AuNPs, which form non-volatile dihexadecyl disulfide upon heating, become liquid at 56 °C. This temperature corresponds to the melting point of dihexadecyl disulfide. In contrast, no liquid phase was observed for BT@AuNPs at any temperature. The stabilising ligands also had a significant influence on the electrical resistances of the AuNP films. The longer HDT ligands imparted resistances of > 100 MΩ at room temperature whilst BT@AuNP films had resistances in the kΩ range. Upon heating, both types of films showed a decrease in resistance. In the case of BT@AuNP films, the resistance did not return to that of the as-formed films. SAXS data showed that the BT@AuNPs do not coarsen until ~ 140 °C whilst HDT@AuNPs underwent changes at lower temperatures (~ 90 °C) that we ascribe to the liquid phase in which the particles were embedded.

Acknowledgements

Author contributions

Paige Summers, Alexander Angeloski, Michael Cortie, and Andrew McDonagh contributed to the study conception and design. Material preparation was by Paige Summers. Data collection and analysis were performed Paige Summers, Alexander Angeloski, Michael Cortie, and Richard Wuhrer. The first draft of the manuscript was written by Paige Summers and Andrew McDonagh and all authors contributed to versions of the manuscript. All authors read and approved the final manuscript.

Funding

Data availability

The authors declare that the data supporting the findings of this study are available within the paper and its Supplementary Information files. Raw data files are available from the corresponding author upon reasonable request.

Declarations

Competing interests   The authors have no relevant financial or non-financial interests to disclose.

Supplementary Information   The online version contains supplementary material available at https://doi.org/10.1007/s10854-025-15854-0.

References

1. J. Im, C. Heaton, N.R.E. Putri, C. Liu, J. Usuba, K. Butler et al., Adv. Sci. (2025). https://doi.org/10.1002/advs.202415496

2. J.A.-O. Im, G.A.-O.X. Trindade, T.A.-O. Quach, A.A.-O. Sohaib, F.A.-O. Wang, J.A.-O. Austin, et al., ACS App. Nano Mat. **5,** 6708–16. (2022) https://doi.org/10.1021/acsanm.2c00742

3. R. Klajn, K.J.M. Bishop, M. Fialkowski, M. Paszewski, C.J. Campbell, T.P. Gray et al., Science **316**, 261–264 (2007)

4. J.V. Alemán, A.V. Chadwick, J. He, M. Hess, K. Horie, R.G. Jones, et al., Pure Appl. Chem. **79**, 1801–29 (2007). https://doi.org/10.1351/pac200779101801

5. M. Zamani, C. Klapperich, A. Furst, Lab Chip (2023). https://doi.org/10.1039/D2LC00552B

6. D. Huang, F. Liao, S. Molesa, D. Redinger, V. Subramanian, J. Electrochem. Soc. **150**, G412–G7 (2003)

7. A. Tirkey, P.J. Babu, Sensors Int. **5**, 100252 (2024). https://doi.org/10.1016/j.sintl.2023.100252

8. D.-B. Grys, B. de Nijs, A.R. Salmon, J. Huang, W. Wang, W.-H. Chen et al., ACS Nano **14**, 8689–8696 (2020)

9. R. Ortega-Córdova, K. Sánchez-Carillo, S. Carrasco-Saavedra, G. Ramírez-García, M.G. Pérez-García, J.F.A. Soltero-Martínez et al., RSC Applied Interfaces **1**, 600–611 (2024)

10. S. Ngernpimai, T. Puangmali, A. Kopwitthaya, P. Tippayawat, A. Chompoosor, S. Teerasong, ACS Appl. Nano Mater. **7**, 13124–13133 (2024)

11. S.R. King, S. Shimmon, D.D. Totonjian, A.M. McDonagh, J. Phys. Chem. C **121**, 13944–13951 (2017)

12. S.R. King, S. Shimmon, A.R. Gentle, M.T. Westerhausen, A. Dowd, A.M. McDonagh, Nanotechnology **27**, 215702 (2016)

13. M.J. Coutts, M.B. Cortie, M.J. Ford, A.M. McDonagh, J. Phys. Chem. C **113**, 1325–1328 (2009)

14. M.B. Cortie, M.J. Coutts, C. Ton-That, A. Dowd, V.J. Keast, A.M. McDonagh, J. Phys. Chem. C **117**, 11377–11384 (2013)

15. P.K. Summers, A. Angeloski, R. Wuhrer, M.B. Cortie, A.M. McDonagh, Phys. Chem. Chem. Phys. **25**, 7170–7175 (2023)

16. P. Summers, R. Wuhrer, A. McDonagh, J. Nanopart. Res. (2024). https://doi.org/10.1007/s11051-024-06012-4

17. J.E. Martin, J. Odinek, J.P. Wilcoxon, R.A. Anderson, P. Provencio, J. Phys. Chem. B **107**, 430–434 (2003)

18. J.R. Reimers, M.J. Ford, A. Halder, J. Ulstrup, N.S. Hush, Proc. Natl. Acad. Sci. U. S. A. **113**, E1424–E33 (2016)

19. B.L. Smith, J.E. Hutchison, J. Phys. Chem. C **117**, 25127–25137 (2013)

20. S.R. King, A.R. Gentle, M.B. Cortie, A.M. McDonagh, J. Phys. Chem. C. **122**, 12098–105 (2018). https://doi.org/10.1021/acs.jpcc.8b02744

21. W.P. Wuelfing, S.J. Green, J.J. Pietron, D.E. Cliffel, R.W. Murray, J. Am. Chem. Soc. **122**, 11465–11472 (2000). https://doi.org/10.1021/ja002367+

22. N.J. Hardy, M.D. Hanwell, T.H. Richardson, J. Mater. Sci. Mater. Electron. **18**, 943–949 (2007)

23. P.K. Summers, R. Wuhrer, A.M. McDonagh, J. Nanopart. Res. **26**, 97 (2024)

24. S.R. King, J. Massicot, A.M. McDonagh, Metals. **5**, 1454–61 (2015). https://doi.org/10.3390/met5031454

25. Y. Wu, Y. Li, P. Liu, S. Gardner, B.S. Ong, Chem. Mater. **18**, 4627–4632 (2006). https://doi.org/10.1021/cm0611643

26. S. Link, M.A. El-Sayed, J. Phys. Chem. B **103**, 4212–4217 (1999)

27. D. Philip, Spectrochim. Acta. A. Mol. Biomol. Spectrosc. **71**, 80–85 (2008). https://doi.org/10.1016/j.saa.2007.11.012

28. M. Brust, D. Bethell, C.J. Kiely, D.J. Schiffrin, Langmuir **14**, 5425–5429 (1998)

29. R.H. Terrill, T.A. Postlethwaite, C.-h Chen, C.-D. Poon, A. Terzis, A. Chen et al., J. Am. Chem. Soc. **117**, 12537–12548 (1995). https://doi.org/10.1021/ja00155a017

30. A. Badia, S. Singh, L. Demers, L. Cuccia, G.R. Brown, R.B. Lennox, Chem. Eur. J. **2**, 359–363 (1996). https://doi.org/10.1002/chem.19960020318

31. A. Badia, L. Cuccia, L. Demers, F. Morin, R.B. Lennox, J. Am. Chem. Soc. **119**, 2682–2692 (1997)

32. X. Chen, J. Schröder, S. Hauschild, S. Rosenfeldt, M. Dulle, S. Förster, Langmuir **31**, 11678–11691 (2015)

33. X. Chen, J. Wang, R. Pan, S. Roth, S. Förster, J. Phys. Chem. C **125**, 1087–1095 (2021)

34. X. Chen, M. Wei, S. Jiang, S. Förster, Langmuir **35**, 12130–12138 (2019)

35. T. Rattanawongwiboon, S. Soontaranon, K. Hemvichian, P. Lertsarawut, S. Laksee, R. Picha, Radiat. Phys. Chem. **191**, 109842 (2022). https://doi.org/10.1016/j.radphyschem.2021.109842